Digest Journal of Nanomaterials and Biostructures Vol. 19, No. 3, July -September 2024, p. 1333 - 1344

# In situ synthesis of $FeNi_3$/$(Fe,Ni)_9S_8$/$Ni_4S_3$/C nanorods and enhancement of oxygen evolution reaction properties

T. Li[a,*], S. Ling[a], S. J. Zhong[a], J. H. Chen[a], M. L. Li[b], Y. Sun[a]
[a]*School of Mechanical Engineering, Chengdu University, Chengdu 610106, China*
[b]*Department of Rehabilitation Medicine, Southwest Medical University, Luzhou 646000, China*

NiFe-based nanomaterials have emerged as highly promising catalysts to replace platinum, ruthenium and iridium for oxygen evolution reaction (OER), in "green hydrogen" production process through water splitting. Using iron (2+) sulfate and nickel acetate as the raw materials, with the molar ratio of Ni acetate to iron (2+) sulfate controlled at 8:5, the concentration of metal-ion was 0.6 mol/L, and precursor fibers rich in $Ni^{2+}$, $Fe^{2+}$, and $SO_4^{2-}$ were prepared using electrospinning technology, with polyvinyl alcohol acting as the colloid. Subsequently, composite nanorods rich in the elements of Ni, Fe, S, and C were successfully obtained at a heat treatment temperature of 1000°C in an Ar gas atmosphere. The results demonstrate that the nanorod samples possessed a surface diameter of ~200 nm, and the main phases of the nanorods after heat treatment at 1000°C included $FeNi_3$ alloy, $(Fe,Ni)_9S_8$, $Ni_4S_3$, and amorphous C. Electrochemical performance tests conducted in a 1.0 mol/L KOH solution exhibited excellent oxygen evolution reaction properties of the catalysts prepared using $FeNi_3$/$(Fe,Ni)_9S_8$/$Ni_4S_3$/C nanorods as the materials. The overpotential was about 258.6 mV of the catalyst material at 10 $mA \cdot cm^{-2}$.

(Received May 18, 2024; Accepted September 20, 2024)

*Keywords:* Nanorods, $FeNi_3$, OER, Synergy enhancement

## 1. Introduction

The problem about the increasing energy demand by social development and the depletion of fossil fuel resources is becoming increasingly serious. So, it is very necessary to vigorously explore renewable energy of solar and hydrogen energy [1]. Among them, hydrogen energy has emerged as a highly promising green energy solution owing to its zero emissions and high calorific value [2-4]. The combination of water splitting and renewable energy is considered a zero-carbon method for hydrogen production because it does not rely on fossil fuels or produce carbon dioxide emissions and is an environmentally friendly and cost-effective renewable energy production technology [5-7]. In order to change the dependence on noble metal catalyst in water electrolysis process [7-12], the exploration of low cost and efficient OER catalysts has become an important research topic.

Studies have proven that transition metal iron and nickel have excellent catalytic properties, and Fe–Ni alloy systems are considered the most promising OER catalysts [13-16]. The d-band theory considered that transition metal alloying can improve the efficiency and density of active centers while adjusting the oxygen adsorption energy to promote water-splitting catalytic activity [17-19]. Therefore, the preparation of binary and multielement alloys, oxides, and hydroxides as

* Corresponding author: litao@cdu.edu.cn
https://doi.org/10.15251/DJNB.2024.193.1333

well as multielement compounds from Fe and Ni transition metals has become the main method for non-noble metal–based catalysts, such as NiFe [15, 20-22], NiCuFeP [23], FeCoNiCuPd [24], $Ni(OH)_2$ [25], Ni/NiO-Pd [11], $Ni_3Fe1Ox@C$ [26], and NiFe-layered double hydroxide (LDH) [20, 27, 28]. Studies also indicate that catalytic activity can be enhanced through the regulation of internal structures, such as nanoclusters [25], nanoporous structures [29], and nano-three-dimensional frameworks [30]. Furthermore, the effective doping of nonmetals such as P, N, and S to form heterojunctions is an even more effective method for improving catalytic activity [21, 23, 31-36].

According to the literature, the catalysts prepared by different processes have a variety of structural forms, and also exhibit very different OER properties at a level of 10 mA $cm^{-2}$. The overpotential of the samples is all in the range of 200-300mV, showing lower OER overpotential and excellent electrocatalytic performance. The OER properties of some reference samples are shown in Table 1. The wide application of NiFe-based alloys and their multielement composite catalysts can be attributed to their remarkable chemical stability, excellent electrical conductivity, and redox properties. In addition, heterostructure materials possess a high active surface area and electron effect, which can effectively improve electronic transmission efficiency [33].

*Table 1. OER properties of some reference samples.*

| Serial number | Sample | Overpotential/ mV | Current density/ mA $cm^{-2}$ | References |
|---|---|---|---|---|
| 1 | $(Ni,Fe)S_2@MoS_2$ core–shell heterostructure | 270 | 10 | [32] |
| 2 | $FeNi_3N–Ni_3S_2$ | 230 | 10 | [33] |
| 3 | NiFe LDH nanoplates | 210 | 10 | [34] |
| 4 | $Ni_3S_2–Co_9S_8$ heterostructure fibers | 294 | 20 | [35] |
| 5 | $Fe(OH)_3/Ni_9S_8$ nanoarray | 206 | 10 | [36] |

In this study, we introduced a new systematic strategy for preparing a composite catalyst material with a loose porous structure. We extensively investigated the microstructure, element states, and electrochemical properties and provided a technical reference for low-cost, convenient, and safe production of NiFe-based catalysts for water decomposition.

## 2. Experimental

### 2.1. Preparation of NiFe catalysts

The process of preparing sample electrode material is shown in Fig. 1. A colorless transparent sol of polyvinyl alcohol (PVA) was prepared and stand for 24 hours to let all the bubbles out. $Ni(CH_3COO)_2·4H_2O$ and $FeSO_4·7H_2O$ were added into the PVA solution, and a light green sol was obtained. The total ion concentration of $Ni^{2+}$ + $Fe^{2+}$ was 0.6 mol/L. A spinning solution was drawn into a syringe and fixed onto the groove of the sampler for electrospinning, with the voltage was 25 KV. The precursor fibers was dried at 95°C for 12 h, nickel acetate/iron (2+) sulfate/PVA

composite nanofiber precursors were obtained. The composite nanofiber precursors were heat-treated in a furnace filled with Ar gas, the temperature was controlled at 400, 600, 800 and 1000°C, respectively, and held for 40 min. After cooling, a set of carbon-based nanomaterials rich in nickel, iron, and sulfur were obtained. The working electrodes of the samples were prepared using a general method, and the OER properties of the sample were tested in a 1.0 mol/L KOH solution.

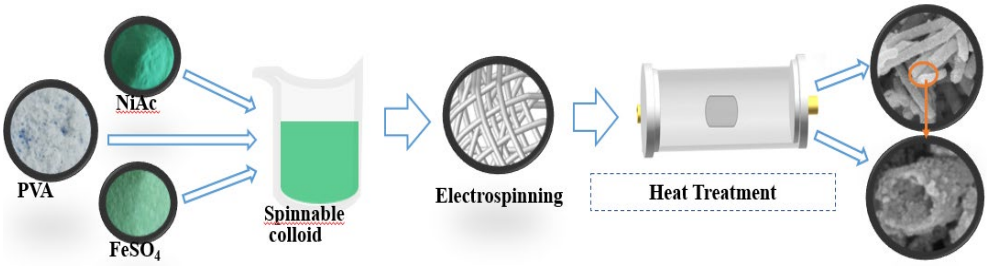


*Fig. 1. Preparation process of the samples.*

### 2.2. Characterizations

The phase and crystal structures were measured using XRD technology (DX-2700B, Dandong Haoyuan) with 40 kV and 30 mA. The morphology was examined using SEM method (Ultra 55, Zeiss). The structural properties of carbon were measured through Raman spectroscopy (Invia, Renishaw). The surface chemical state was determined by XPS method (Thermo Scientific K-Alpha). The BET was measured using a specific surface area analyzer (V-Sorb 2800P). The electrochemical properties were measured using an electrochemical workstation (CS350M, Costa).

## 3. Results and discussions

### 3.1. XRD analysis

The XRD patterns of samples are shown as Fig. 2. After the precursor was calcined at 400°C (S-400) and 600°C (S-600) (Fig. 2), no obvious $FeNi_3$ diffraction peak was visible. However, three main peaks at 44.51°, 51.85°, and 76.37°, which according to the PDF#04-0850 card of Ni metal. When the precursor was calcined at 800°C (S-800) and 1000°C (S-1000), the spectra of the samples showed obvious diffraction peaks of $FeNi_3$ at 44.28°, 51.53°, and 75.87°, corresponding to the PDF#38-0419 card. The XRD pattern of S-800 showed faint peaks of sulfide $(Fe, Ni)_9S_8$ corresponding to the PDF#08-0090 card; however, no obvious diffraction peaks of $Ni_4S_3$ Were visible. The XRD pattern of S-1000 showed obvious diffraction peaks of $(Fe, Ni)_9S_8$ at 29.45°, 31.44°, 47.02°, and 72.22°, corresponding to the PDF#08-0090 card. Moreover, S-1000 showed diffraction peaks of $Ni_4S_3$ at 30.14° and 50.17°, corresponding to the PDF#52-1027 card; however, no obvious diffraction peaks of Ni were visible. From the XRD results we can get a conclusion that the main components of the samples S-1000 are $FeNi_3$, $(Fe, Ni)_9S_8$, $Ni_4S_3$, and C.

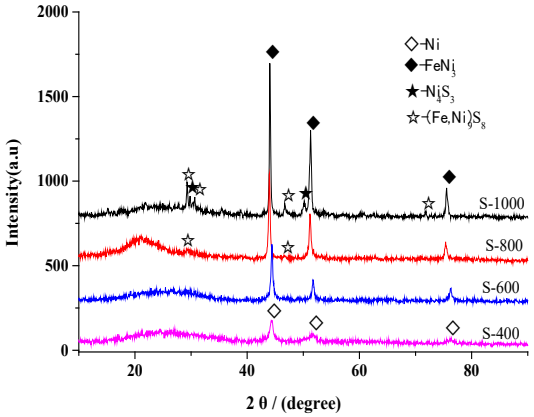


*Fig. 2. XRD pattern of samples.*

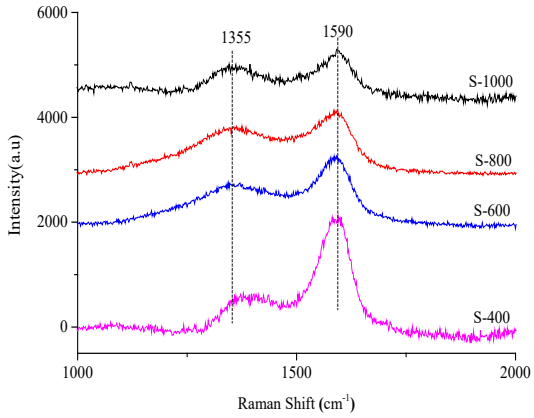


*Fig. 3. Raman pattern of samples.*

### 3.2. Raman analysis

The Raman pattern Fig. 3 of samples shows two main peaks at about 1355 and 1590 $cm^{-1}$. The peak near 1355 $cm^{-1}$ corresponding to the characteristic peaks of D-band, which is induced by structural defects. Another peak near 1590 $cm^{-1}$ according to the characteristic peaks of G-band, which is induced by C $sp^2$ hybridization. Usually the $I_D/I_G$ ratio is used for estimating the situation of defects in carbon materials [37]. The $I_D/I_G$ ratios of the samples as prepared were 0.32 (S-400), 0.56(S-600), 0.81(S-800), and 0.71(S-1000), which show that the higher the heat treatment temperature, the greater the defect degree of the sample. The metal elements and crystal grains contributes to an increase in the degree of defects as the temperature increases. The prepared composite catalyst exhibited satisfactory electrocatalytic performance owing to the large defects in amorphous C and the interaction between the metal elements and S.

### 3.3. Morphology and mapping analysis

The morphology characterization of samples as prepared are shown in Fig. 4. As shown in Fig. 4(a), the sample heat-treated at 400°C exhibits a complete rod-shape with a smooth surface, a dense internal structure, and some instances of rod adhesion. Fig. 4(b) shows that the sample heat-treated at 600°C exhibits a complete rod shape, and the surface of the nanorods becomes rougher

and exhibits a distinct graininess, whereas the internal texture becomes relatively dense. The rods become loosely dispersed and no longer adhere together. Fig. 4(c) shows that the sample S-800 has a complete rod shape with a very loose and independent rod-to-rod relation, with the diameter 100–200 nm, and the surface becomes very rough, with obvious particle formation. The inner texture of the sample is no longer dense, and small holes are obvious on the surface and cross-section of the nanorods, which was marked with red circle. Fig. 4(d) shows that the surface of the nanorods heat-treated at 1000°C is rougher, and the inner part of the nanorods is hollow and becomes a nanotube shape (marked as A and B) with a diameter about 100–200 nm. Fig. 4(d) also shows that some nanorod shapes are no longer complete, some have broken into arc-shaped nanosheets (marked with letter C), or some have disintegrated (marked with letter D).

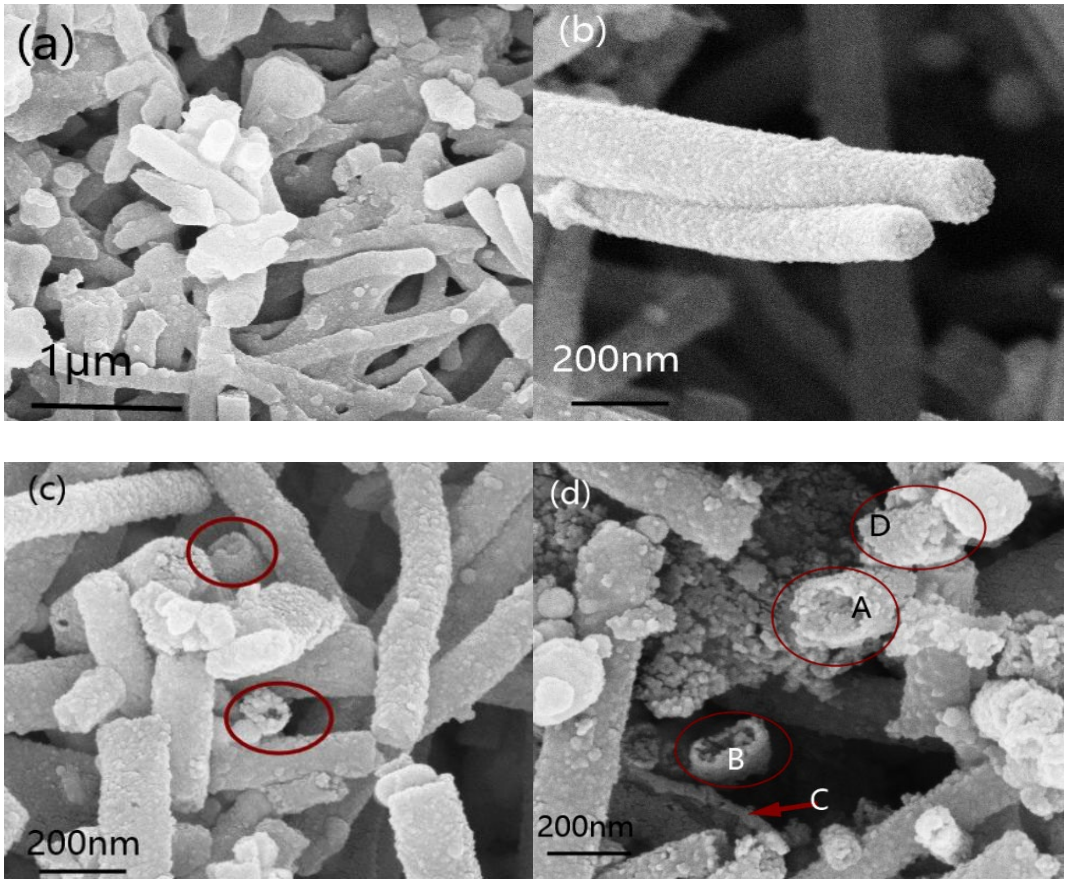


*Fig. 4. SEM photos of samples: (a) S-400, (b) S-600, (c) S-800, and (d) S-1000.*

The element distribution mappings of $FeNi_3$/(Fe, Ni)$_9S_8$/$Ni_4S_3$/C (S-1000) were shown in Fig. 5. The mapping obtained via macro-field scanning were shown as Figs. 5(a1)–5(a4), The mapping of the nanorods selected for the element distribution test was shown as Figs. 5(b1)–5(b4). Fig. 5 Comprehensive analysis shows that Fe, Ni and S are uniformly spread in nanorod.

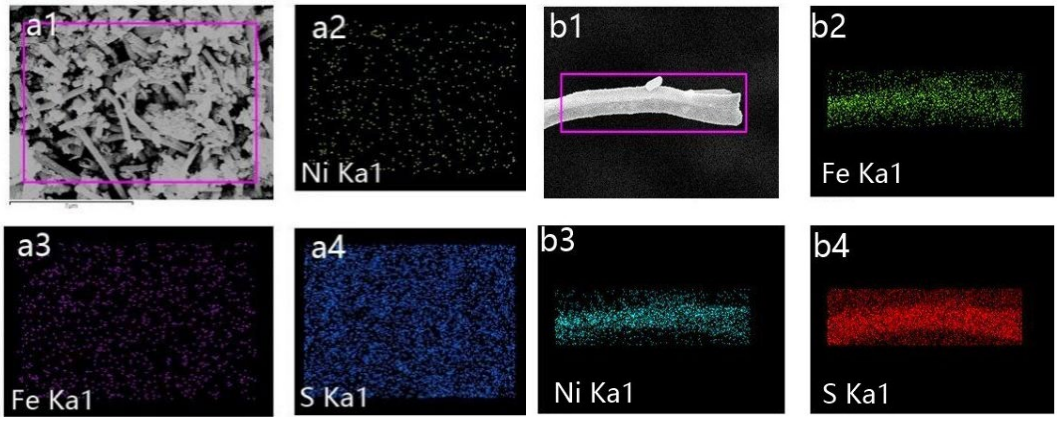


*Fig. 5. Mappings of the S-1000 sample: (a) Field scan and (b) single rod scan.*

Comprehensive analysis of SEM and mapping shows that, with the increases of temperature, the decomposition of the fiber precursor gradually becomes complete, and the loss of elements and gas impact make the sample from dense to porous. The surface and interior of the nanorods of sample S-1000 became porous and Ni, Fe, and S were uniformly distributed in the nanorod body. This can be attributed to the strengthening of the alloying and vulcanization reactions of NiFe as well as the intensified carbonization reaction of the fiber body heat-treated at 1000°C. During the formation of FeNi alloy and sulfide, the structure of fiber body was seriously damaged, resulting in the formation of multielement mixed-crystal nanorods with a hollow porous structure. Because of its hollow and porous structure, $FeNi_3$/(Fe, Ni)$_9S_8$/$Ni_4S_3$/C catalyst has a large specific surface area of 134.6 $m^2\ g^{-1}$, which increases the number of catalytic activity sites and effectively improves the catalytic performance.

### 3.4. XPS analysis

Chemical valence state of $FeNi_3$/(Fe, Ni)$_9S_8$/$Ni_4S_3$/C catalyst (sample S-1000) were measured by XPS technology. Fig. 6(a) shows that Ni, Fe, S, and C are the main elements of S-1000 [15, 26, 35]. The elements of S-1000 consist of C (91.32 at%), Ni (2.83 at%), Fe (2.60 at%), and S (3.26 at%). Fig. 6(b) shows a main peak of sample S-1000 at 284.8 eV corresponds to the characteristic chemical energy of C–C [15, 28, 38]. Fig. 6(c) shows 2p region of Ni divides into two main regions at peaks of 856.3 and 874.6 eV respectively, which corresponding to $Ni^{2+}$ $2p_{3/2}$ and $Ni^{2+}$ $2p_{1/2}$, indicating that Ni is in the $Ni^{2+}$ oxidation state mainly. Furthermore, the satellite peaks located at 862.5 and 879.7 eV, correspond to the Ni 2p. Fig. 6(c) also shows that there are extra two peaks located at 853.4 and 871.7 eV, which corresponding to Ni(II)–S bonds [34, 39]. Fig. 6(d) shows two main peaks at 711.9 and 724.8 eV, corresponding to the $Fe^{3+}$ $2p_{3/2}$ and $Fe^{3+}$ $2p_{1/2}$ regions, respectively. The spectrum of Fe 2p also shows two peaks at 707.9 and 721.1 eV, indicating the formation of Fe(II)–S bonds [34, 39-41]. Fig. 6(e) shows two peaks at 161.9 and 163.9 eV of S $2p_{3/2}$ and S $2p_{1/2}$, respectively, which are consistent with the signals of the divalent sulfide ion ($S^{2-}$) [35, 36, 39, 40]. Fig. 6(e) shows another two peaks at 162.8 and 164.9 eV, which was the signals of superimposition of $S_2^{2-}$ [34]. In addition, Fig. 6(e) shows the S2p core energy level spectra at 168.6 and 169.6 eV, corresponding to the $S2p_{3/2}$ and $S2p_{1/2}$ of $SO_4^{2-}$ [15, 36, 39].

### 3.5. Electrocatalytic properties analysis

The electrocatalytic performance of working electrodes made from samples in water-splitting process was evaluated on an electrochemical workstation. The LSV (linear cyclic voltammetry) curves (Fig. 7(a)) indicates that the electrocatalytic activity of the samples gradually enhances, as the heat treatment temperature increases. Fig. 7(a) also shows that sample S-1000 exhibits considerably better electrocatalytic activity than the other three samples. From Fig. 7(b) we can see that the overpotentials of the samples as-prepared were 368.6 mV (S-400), 309.4 mV (S-600), 289.6 mV (S-800), and 258.6 mV (S-1000), with a gradual downward trend, at a current density of 10 mA $cm^{-2}$. These results demonstrate that the nanocomposite mixed crystal obtained via the heat treatment of the precursor at 1000℃ exhibits excellent catalytic performance.

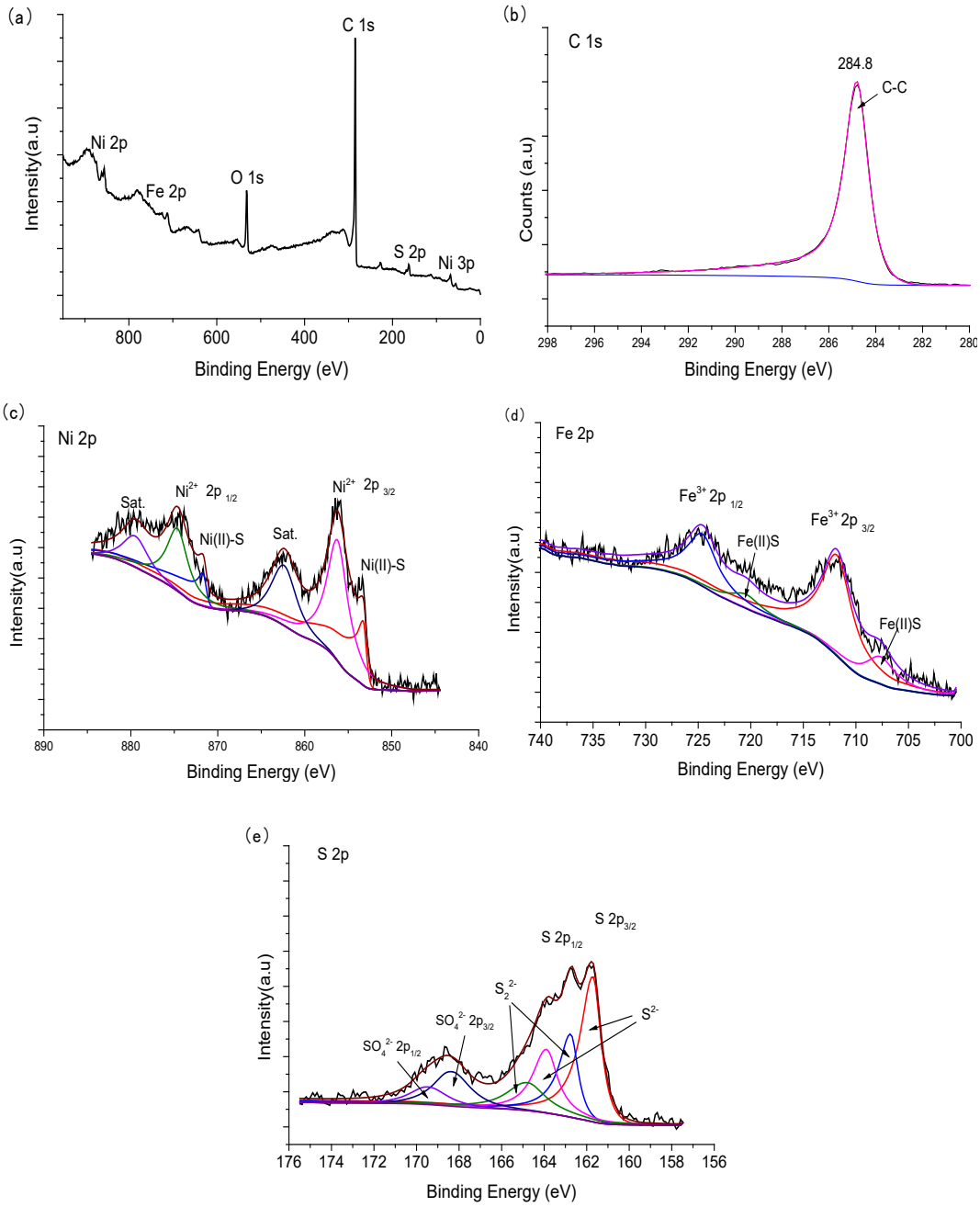


*Fig. 6. XPS spectrum of S-1000: (a) full spectrum, (b) C 1s, (c) Ni 2p, (d) Fe 2p, and (e) S 2p.*

The Tafel slopes dot line chart of catalyst samples was obtained and shown as Fig. 7(c). The values of Tafel slopes were 127.8 (S-400), 109.6 (S-600), 97.4 (S-800), and 68.5 mV $dec^{-1}$ (S-1000), and sample S-1000 exhibits a small Tafel slope. Moreover, the working electrode, prepared from the nanocomposite mixed-crystal sample, after 1000 °C heat treatment demonstrates kinetic advantage and excellent activity [42]. The results indicate that $FeNi_3$/(Fe, Ni)$_9S_8$/$Ni_4S_3$/C catalyst sample has faster rate of multielectron transfer reactions, resulting in a faster oxygen evolution process and higher electrochemical activity [43, 44]. This enhancement effect is due to the nano porous structure and heterojunction, contributing to an electronic effect that enhances catalytic performance [33].

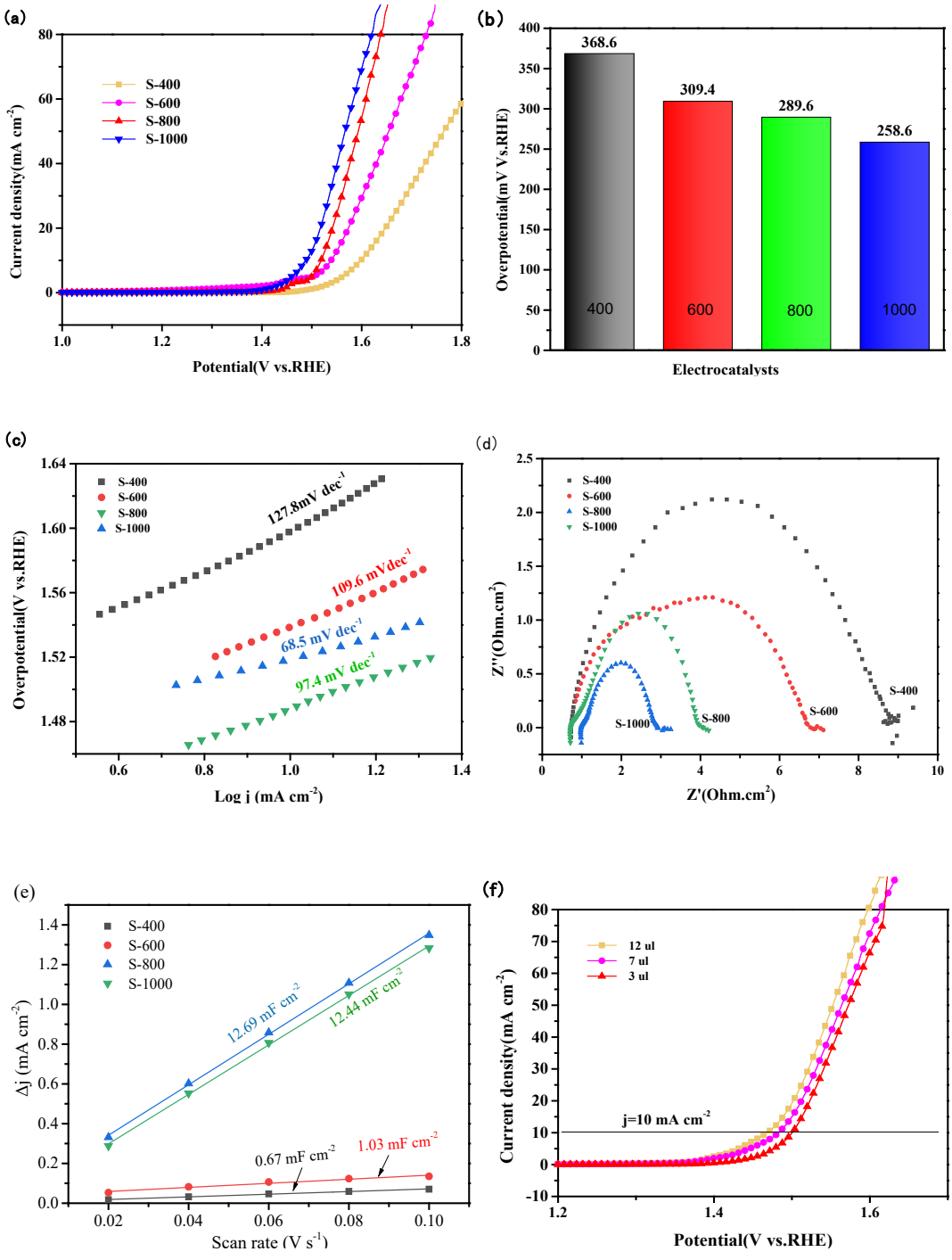

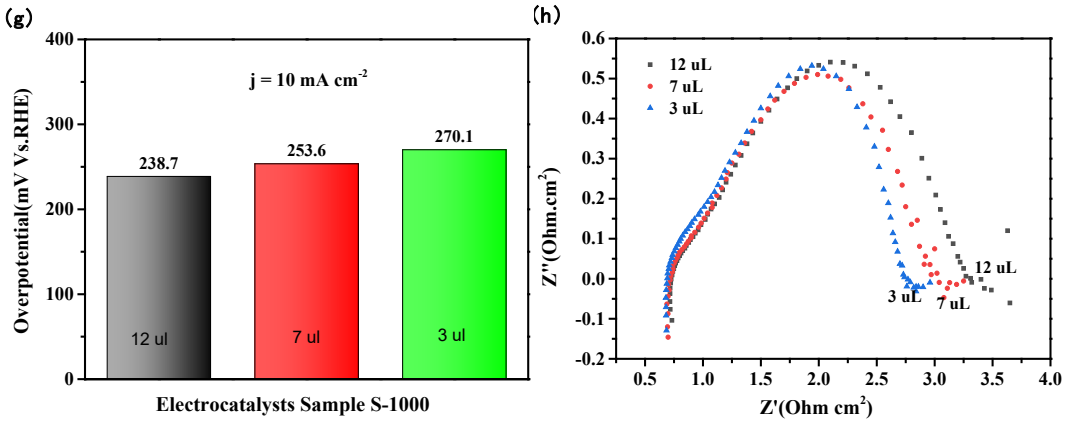


*Fig. 7. Electrochemical properties of samples: (a) LSV curves, (b) overpotentials, (c) Tafel plots, (d) Nyquist diagram, (e) capacitance current and scanning rate, (f) LSV curves of S-1000 with different quantities, (g) overpotentials, and (h) Nyquist diagram.*

The resistance ($R_{ct}$) of the working electrodes during electrocatalytic reaction was tested by measuring the electrochemical impedance. The results in fig. 7(d) indicated that the semi-circular region of the curve has significant differences of the working electrode Nyquist plots. Among the four samples, the working electrode made from sample S-1000 exhibited the smallest semicircle, that is to say, the catalyst sample S-1000 can accelerate the kinetic process and improve the electron transfer ability effectively, in water-splitting reactions. The reason behind this observation is that during the heat treatment process, the raw materials decompose to form nickel, iron, sulfur, and carbon atoms, and mutual diffusion during chemical synthesis accelerates the alloying reaction between elements. The alloying reaction forms a stable heterostructure layer between grains of different elements, thereby improving conductivity and electron transfer efficiency. Therefore, the OER performance of FeNi3/(Fe, Ni) 9S8/Ni4S3/C nanocomposites was enhanced [33, 42].

Fig. 7(e) shows the $C_{dl}$ value of catalysts calculated. The $C_{dl}$ value of $FeNi_3$/(Fe, Ni)$_9S_8$/$Ni_4S_3$/C nanocomposite catalyst was about 12.44 mF cm$^{-2}$, which is considerably better than that of S-400 (0.67 mF cm$^{-2}$) and S-600 (1.03 mF cm$^{-2}$), implying a higher electrochemical surface area of $FeNi_3$/(Fe, Ni)$_9S_8$/$Ni_4S_3$/C. The Brunauer–Emmett–Teller result was 134.6 m$^2$/g of $FeNi_3$/(Fe, Ni)$_9S_8$/$Ni_4S_3$/C sample, supporting its high active surface area.

The effect of catalyst loading on catalytic behavior is shown in Figure Fig. 7(f)–7(h). Fig. 7(f) demonstrates a gradual increase in catalytic activity with increasing catalyst mass; however, the increase is small. Fig. 7(g) shows that the overpotential decreases with increasing catalyst mass to 270.1 mV (3 µL), 253.6 mV (7 µL), and 238.7 mV (12 µL), at 10 mA cm$^{-2}$; however, the extent of the reduction is small. Similarly, the results of charge transfer resistance $R_{ct}$ (Fig. 7(h)) show that the $R_{ct}$ value increases with increasing catalyst mass; however, the extent of the increase is small.

The overpotential about 258.6 mV of $FeNi_3$/(Fe, Ni)$_9S_8$/$Ni_4S_3$/C catalyst at 10 mA cm$^{-2}$ and which can decrease as concentration increases appropriately, shows an excellent electrocatalytic OER performance, which is comparable to the overpotential value reported in Refs. [32-36] and superior to that in Refs. [32, 35].

## 4. Conclusion

Herein, a technical proposal was designed for preparing mixed-crystal composite nanomaterials rich in the elements of Ni, Fe, S, and C, through electrospinning and atmosphere heat treatment techniques. This one-step process involved alloying, carbonization, and vulcanization of composite nanomaterials containing multiphase sulfides ($(Fe,Ni)_9S_8$ and $Ni_4S_3$) and $FeNi_3$. Thus, porous hollow $FeNi_3/(Fe,Ni)_9S_8/Ni_4S_3/C$ composite nanorods were successfully prepared. This approach enabled a simple, reliable, and systematic strategy for developing and employing FeNi–based catalysts with outstanding OER performance.

The chemical components of $FeNi_3/(Fe,Ni)_9S_8/Ni_4S_3/C$ composite nanorods were influenced by the heat treatment temperature. With increasing heat treatment temperature, the alloying reaction of Ni, Fe, and S in the composite nanorods became more intense, resulting in stronger element binding, more complete crystal grains, and a more stable heterojunction. As a result, the electrocatalytic reaction were improved.

$FeNi_3/(Fe, Ni)_9S_8/Ni_4S_3/C$ mixed-crystalline composite nanorods prepared at 1000°C in Ar gas atmosphere, exhibited excellent OER performance in an alkaline solution. The $FeNi_3/(Fe,Ni)_9S_8/Ni_4S_3/C$ electrode exhibited excellent OER activity during the water-splitting process.

### Acknowledgments

This research work was funded by the Sichuan Science and Technology Program (2023YFG0229).

## References

[1] D. J. Larcher, J. M. Tarascon, Nature Chemistry 7(1), 19 (2015); https://doi.org/10.1038/nchem.2085

[2] C. Yang, G. Rousse, K. Louise Svane, P. E. Pearce, A. M. Abakumov, M. Deschamps, G. Cibin, A. V. Chadwick, D. A. Dalla Corte, H. Anton Hansen, T. Vegge, Nature Communications 11(1), 1378 (2020); https://doi.org/10.1038/s41467-020-15231-x

[3] H. Wang, K. H. L. Zhang, J. P. Hofmann, F. E. Oropeza, Journal of Materials Chemistry A 9(35), 19465 (2021); https://doi.org/10.1039/D1TA03732C

[4] Z. Y. Wu, F. Y. Chen, B. Li, S. W. Yu, Y. Z. Finfrock, D. M. Meira, Q. Q. Yan, P. Zhu, M. X. Chen, T. W. Song, Z. Yin, Nature Materials 22(1), 100 (2023); https://doi.org/10.1038/s41563-022-01380-5

[5] Z. Y. Yu, Y. Duan, X. Y. Feng, X. Yu, M. R. Gao, S. H. Yu, Advanced Materials 33(31), 2007100 (2021); https://doi.org/10.1002/adma.202007100

[6] A. Loh, X. Li, O. O. Taiwo, F. Tariq, N. P. Brandon, P. Wang, K. Xu, B. Wang, International Journal of Hydrogen Energy 45(46), 24232 (2020); https://doi.org/10.1016/j.ijhydene.2020.06.253

[7] J. Feng, F. Lv, W. Zhang, P. Li, K. Wang, C. Yang, B. Wang, Y. Yang, J. Zhou, F. Lin, G. C.

Wang, Advanced Materials 29(47), 1703798 (2017); https://doi.org/10.1002/adma.201703798

[8] C. Cui, L. Gan, M. Heggen, S. Rudi, P. Strasser, Nature Materials 12(8), 765 (2013); https://doi.org/10.1038/nmat3668

[9] Q. Cheng, C. Hu, G. Wang, Z. Zou, H. Yang, L. Dai, Journal of the American Chemical Society 142(12), 5594 (2020); https://doi.org/10.1021/jacs.9b11524

[10] W. Li, Y. Liu, M. Wu, Feng X, S. A. Redfern, Y. Shang, X. Yong, T. Feng, K. Wu, Z. Liu, B. Li, Advanced Materials 30(31), 1800676 (2018); https://doi.org/10.1002/adma.201800676

[11] A. Barhoum, H. H. El-Maghrabi, I. Iatsunskyi, E. Coy, A. Renard, C. Salameh, M. Weber, S. Sayegh, A. A. Nada, S. Roualdes, M. Bechelany, Journal of Colloid and Interface Science 569, 286 (2020); https://doi.org/10.1016/j.jcis.2020.02.063

[12] L. Zu, X. Qian, S. Zhao, Q. Liang, Y. E. Chen, M. Liu, B. J. Su, K. H. Wu, L. Qu, L. Duan, H. Zhan, Journal of the American Chemical Society 144(5), 2208 (2022); https://doi.org/10.1021/jacs.1c11241

[13] J. Peng, W. Dong, Z. Wang, Y. Meng, W. Liu, P. Song, Z. Liu, Materials Today Advances 8, 100081 (2020); https://doi.org/10.1016/j.mtadv.2020.100081

[14] M. Yu, E. Budiyanto, H. Tüysüz, Angewandte Chemie International Edition 61(1), e202103824 (2022); https://doi.org/10.1002/anie.202103824

[15] J. W. Zhang, H. Zhang, T. Z. Ren, Z. Y. Yuan, T. J. Bandosz, Frontiers of Chemical Science and Engineering 15, 279 (2021); https://doi.org/10.1007/s11705-020-1965-2

[16] H. Khani, N. S. Grundish, D. O. Wipf, J. B. Goodenough, Advanced Energy Materials 10(1), 1903215 (2020); https://doi.org/10.1002/aenm.201903215

[17] Y. Pi, Q. Shao, P. Wang, J. Guo, X. Huang, Advanced Functional Materials 27(27), 1700886 (2017); https://doi.org/10.1002/adfm.201700886

[18] H. K. Park, H. Ahn, T. H. Lee, J. Y. Lee, M. G. Lee, S. A. Lee, J. W. Yang, S. J. Kim, S. H. Ahn, S. Y. Kim, C. H. Lee, Small Methods 5(2), 2000755 (2021); https://doi.org/10.1002/smtd.202000755

[19] J. R. Kitchin, J. K. Nørskov, M. A. Barteau, J. G. Chen, Physical Review Letters 93(15), 156801 (2004); https://doi.org/10.1103/PhysRevLett.93.156801

[20] J. Mohammed-Ibrahim, Journal of Power Sources 448, 227375 (2020); https://doi.org/10.1016/j.jpowsour.2019.227375

[21] T. Li, S. Zhong, Q. Lou, S. Ling, J. Chen, G. Ma, M. Yang, X. Wu, Journal of Wuhan University of Technology-Materials Science Edition 38(2), 267 (2023); https://doi.org/10.1007/s11595-023-2692-6

[22] D. Lim, E. Oh, C. Lim, S. E. Shim, S. H. Baeck, Catalysis Today 352, 27 (2020); https://doi.org/10.1016/j.cattod.2019.09.046

[23] J. Jin, J. Ge, X. Zhao, Y. Wang, F. Zhang, X. Lei, Inorganic Chemistry Frontiers 9(7), 1446 (2022); https://doi.org/10.1039/D1QI01537K

[24] S. Wang, B. Xu, W. Huo, H. Feng, X. Zhou, F. Fang, Z. Xie, J. K. Shang, J. Jiang, Applied Catalysis B: Environmental 313, 121472 (2022); https://doi.org/10.1016/j.apcatb.2022.121472

[25] N. Danilovic, R. Subbaraman, D. Strmcnik, K. -C. Chang, A. P. Paulikas, V. R. Stamenkovic, N. M. Markovic, Angewandte Chemie 124(50), 12663 (2012); https://doi.org/10.1002/anie.201204842

[26] X. Bai, Y. Ma, Q. Wang, J. Guan, International Journal of Hydrogen Energy 47(4), 2304 (2022); https://doi.org/10.1016/j.ijhydene.2021.10.119

[27] Y. Zhou, Z. Wang, Z. Pan, L. Liu, J. Xi, X. Luo, Y. Shen, Advanced Materials 31(8), 1806769 (2019); https://doi.org/10.1002/adma.201806769

[28] J. Miao, X. Zhao, H. Y. Hu, Z. H. Liu, Colloids and Surfaces A: Physicochemical and Engineering Aspects 635, 128092 (2022); https://doi.org/10.1016/j.colsurfa.2021.128092

[29] J. T. Ren, Y. Yao, Z. Y. Yuan, Green Energy & Environment 6(5), 620 (2021); https://doi.org/10.1016/j.gee.2020.11.023

[30] C. Zhang, X. Shen, Y. Pan, Z. Peng, Frontiers in Energy 11, 268 (2017); https://doi.org/10.1007/s11708-017-0466-6

[31] J. Chang, S. Zang, J. Li, D. Wu, Z. Lian, F. Xu, K. Jiang, Z. Gao, Electrochimica Acta 389, 138785 (2021); https://doi.org/10.1016/j.electacta.2021.138785

[32] Y. Liu, S. Jiang, S. Li, L. Zhou, Z. Li, J. Li, M. Shao, Applied Catalysis B: Environmental 247, 107 (2019);https://doi.org/10.1016/j.apcatb.2019.01.094

[33] S. Liang, M. Jing, E. Pervaiz, H. Guo, T. Thomas, W. Song, J. Xu, A. Saad, J. Wang, H. Shen, J. Liu, ACS Applied Materials & Interfaces 12(37), 41464 (2020); https://doi.org/10.1021/acsami.0c11324

[34] Y. Zou, B. Xiao, J. W. Shi, H. Hao, D. Ma, Y. Lv, G. Sun, J. Li, Y. Cheng, Electrochimica Acta 348, 136339 (2020); https://doi.org/10.1016/j.electacta.2020.136339

[35] R. Zhang, L. Cheng, Z. Wang, F. Kong, Y. Tsegazeb, W. Lv, W. Wang, Applied Surface Science 526, 146753 (2020); https://doi.org/10.1016/j.apsusc.2020.146753

[36] X. Chen, X. Wang, X. Zhang, K. Srinivas, D. Liu, X. Zhao, H. Yu, B. Wang, W. Zhang, Y. Chen, Journal of Materials Science 56(34), 19144 (2021); https://doi.org/10.1007/s10853-021-06460-6

[37] O. A. Fakayode, B. A. Yusuf, C. Zhou, Y. Xu, Q. Ji, J. Xie, H. Ma, Energy Conversion and Management 227, 113628 (2021); https://doi.org/10.1016/j.enconman.2020.113628

[38] T. Ma, M. Yuan, S. M. Islam, H. Li, S. Ma, G. Sun, X. Yang, Journal of Alloys and Compounds 678, 468 (2016); https://doi.org/10.1016/j.jallcom.2016.03.243

[39] Q. Wu, S. Wang, J. Guo, X. Feng, H. Li, S. Lv, Y. Zhou, Z. Chen, Nano Research 15(3), 1901 (2022); https://doi.org/10.1007/s12274-021-3800-6

[40] Y. Chen, S. Xu, Y. Li, R. J. Jacob, Y. Kuang, B. Liu, Y. Wang, G. Pastel, L. G. Salamanca-Riba, M. R. Zachariah, L. Hu, Advanced Energy Materials 7(19), 1700482 (2017); https://doi.org/10.1002/aenm.201700482

[41] J. Liu, J. Zhou, S. Liu, G. Chen, W. Wu, P. Jin, C. Xu, Electrochimica Acta 356, 136827 (2020); https://doi.org/10.1016/j.electacta.2020.136827

[42] M. Zhong, N. Song, C. Li, C. Wang, W. Chen, X. Lu, Journal of Colloid and Interface Science 614, 556 (2022); https://doi.org/10.1016/j.jcis.2022.01.134

[43] S. Anantharaj, V. Aravindan, Advanced Energy Materials 10(1), 1902666 (2020); https://doi.org/10.1002/aenm.201902666

[44] X. Shi, X. Ling, L. Li, C. Zhong, Y. Deng, X. Han, W. Hu, Journal of Materials Chemistry A 7(41), 23787 (2019); https://doi.org/10.1039/C9TA03819A